Marine Micropaleontology 201 (2025) 102525

Contents lists available at ScienceDirect

Marine Micropaleontology

journal homepage: www.elsevier.com/locate/marmicro

Research paper

Size variation of *Eprolithus floralis* across Oceanic Anoxic Event 2 (Late Cretaceous) in the Eastbourne section

Edna de Jesus Francisco Tungo [a,b], Elisabetta Erba [c], Gerson Fauth [a,b], Cinzia Bottini [c,*]

[a] Post – Graduate Program in Geology, Universidade do Vale do Rio dos Sinos – UNISINOS University, São Leopoldo, Rio Grande do Sul, Brazil
[b] ITT Oceaneon – Instituto Tecnológico de Paleoceanografia e Mudanças Climáticas, Unisinos University, São Leopoldo, Brazil
[c] Dipartimento di Scienze della Terra "Ardito Desio", Università Degli Studi Di Milano, Milano, Italy

ARTICLE INFO

Keywords:
Eprolithus floralis
Nannofossils
Morphometry
OAE 2
Cenomanian/Turonian
Plenus Cold Event

ABSTRACT

Morphometric analyses of *Eprolithus floralis* were conducted in the Eastbourne section (southeast England, UK) to quantify size changes of this nannofossil species across Oceanic Anoxic Event 2 (OAE 2; Cenomanian/Turonian boundary, ~94 Ma). The total and inner diameters exhibit a reduction of 3 % and 2.4 %, respectively, relative to the overall mean size during OAE 2 with minimum values (~1 μm smaller) occurring at carbon isotope peak B. A recovery of 8.4 % and 5.7 % in two distinct morphotypes were identified: the *rounded* morphotype is ca. 0.5 μm smaller than the *spiky* one and starts to be more abundant just prior to OAE 2. The *spiky* morphotype accounts for 61 % before and 56 % after OAE 2 where it also shows largest average sizes and the smallest diaphragm. Morphometric shifts coincide with the onset of intense volcanism from the Caribbean Plateau whereas the size increase parallels the decline in volcanic activity, suggesting a possible link between environmental recovery and morphological diversification.

Size and abundance minima of *E. floralis* and *Biscutum constans* at peak B suggest a shared physiological response, likely reduced calcification, to maximum environmental stress and possibly ocean acidification. However, *E. floralis* shows earlier size recovery, indicating higher ecological tolerance. No clear correlation is found with the Plenus Cold Event, excluding temperature as a primary control of *E. floralis* abundance and size.

1. Introduction

The Late Cretaceous was marked by a complex environmental perturbation known as Oceanic Anoxic Event 2 (OAE 2; ~94 Ma) (e.g., Schlanger and Jenkyns, 1976; Scholle and Arthur, 1980; Schlanger et al., 1987; Jenkyns, 2010). This event led to widespread oceanic dysoxia/anoxia (e.g., Pancost et al., 2004; Meyer and Kump, 2008; Dickson et al., 2016; Ostrander et al., 2017) evidenced by the deposition of organic C-rich lithologies, such as the Bonarelli Level and its equivalents, which are widely recorded in pelagic and hemipelagic successions (Schlanger and Jenkyns, 1976; Schlanger et al., 1987; Zimmerman et al., 1987; Erba et al., 2019; Robinson et al., 2019). The development of anoxic conditions induced substantial changes in the global carbon cycle (e.g., Bice et al., 2006; Förster et al., 2007; Wagreich et al., 2011; Yao et al., 2021) reflected in the positive carbon-isotope excursion (CIE) that defines the stratigraphic extent of OAE 2 (e.g., Arthur et al., 1988; Tsikos et al., 2004; Voigt et al., 2007, 2008; Jarvis et al., 2011; Owens et al., 2018; Gale et al., 2019; Jones et al., 2023). This excursion comprises four distinct peaks, labeled A to D by Jarvis et al. (2006) and Voigt et al. (2007, 2008).

The primary driver of OAE 2 is attributed to elevated atmospheric CO_2, primarily linked to the activity of the Caribbean Large Igneous Province (LIP), which released vast amounts of greenhouse gases into the ocean-atmosphere system (e.g., Snow et al., 2005; Turgeon and Creaser, 2008; Jarvis et al., 2011; Du Vivier et al., 2014; Percival et al., 2015, 2025; Grasby et al., 2019; Jones et al., 2021). These emissions triggered an abrupt and prolonged warming, contributing to the highest recorded sea-surface temperatures of the Late Cretaceous (e.g., Förster et al., 2007; Sinninghe Damsté et al., 2010; O'Brien et al., 2017; Huber et al., 2018; Macdonald et al., 2019). Volcanic activity and/or basalt-seawater interaction likely played an additional role in enriching seawater with key nutrients, driving substantial biological responses (Orth et al., 1993; Erba, 2004; Snow et al., 2005; Turgeon and Creaser, 2008; Duggen et al., 2010; Langmann et al., 2010; Du Vivier et al., 2014; Jenkyns et al., 2017; Faucher et al., 2017; Jones et al., 2021; Petrizzo et al., 2025).

* Corresponding author.
E-mail address: cinzia.bottini@unimi.it (C. Bottini).

https://doi.org/10.1016/j.marmicro.2025.102525
Received 6 June 2025; Received in revised form 23 September 2025; Accepted 20 October 2025
Available online 27 October 2025
0377-8398/© 2025 The Authors. Published by Elsevier B.V. This is an open access article under the CC BY license (http://creativecommons.org/licenses/by/4.0/).

Thus, OAE 2 represents a crucial case study for understanding the response of organisms to extreme oceanic environmental disruption. This study focuses on calcareous nannoplankton, which is a group highly responsive to environmental changes but also relatively resilient (Erba, 2004; Erba and Parente, 2025). Specifically, we examine the behavior of *Eprolithus floralis* (Stradner, 1962; Stover, 1966), a heavily calcified nannolith belonging to the Polycyclolithaceae Family. *Eprolithus floralis* is known for its affinity to cooler waters and is typically more abundant at higher latitudes (e.g., Roth and Krumbach, 1986; Bralower, 1988; Erba, 1992, 2004; Premoli Silva et al., 1999; Herrle et al., 2003).

Previous studies have demonstrated that some taxa within calcareous nannoplankton underwent size and/or abundance reduction in response to elevated CO_2 concentrations during the Toarcian T-OAE (Faucher et al., 2022 and reference therein), the Weissert OAE (Erba and Tremolada, 2004; Erba et al., 2019; Möller et al., 2020), and the early Aptian OAE 1a (Erba, 1994, 2004; Erba et al., 2010, 2019). Morphometric data are available for a few species across OAE 2 (Faucher et al., 2017), that should be extended to other components of the nannofossil assemblage. We aim to assess whether the response of *E. floralis* parallels that of coccolith-bearing species such as *Biscutum constans* to determine if a common environmental factor influenced their calcification. Previous studies have shown that *B. constans* underwent a global and synchronous size reduction, with maximum dwarfism occurring around peak B of the CIE (Faucher et al., 2017). This reduction has been interpreted as an adaptive strategy to cope with ocean acidification and/or toxic metal influxes (Faucher et al., 2017). Given the affinity of *E. floralis* for cooler waters, we also aim to explore the role, if any, of temperature variations across OAE 2 on its size and abundance.

To address these objectives, we selected the Eastbourne succession (Sussex, England) (Fig. 1), a stratigraphically well constrained reference section for OAE 2 for which morphometric data of *B. constans* are available (Faucher et al., 2017). The Eastbourne section also provides a well-defined record of the Plenus Cold Event (PCE) which represents a transient cooling episode associated with a temporary decline in atmospheric pCO_2 (Kuypers et al., 1999; Voigt et al., 2006; Förster et al., 2007; Barclay et al., 2010; Sinninghe Damsté et al., 2010; Jarvis et al., 2011; Gale et al., 2019; O'Connor et al., 2020) and global-scale bottom-water reoxygenation (Eicher and Worstell, 1970; Eicher and Diner, 1985; Paul et al., 1999; Förster et al., 2007; Keller et al., 2008; Eldrett et al., 2014; Dodsworth, 2016; Bryant et al., 2021; Amaglio et al., 2023) occurred between the second buildup of the CIE (before peak A) and peak B (e.g., Förster et al., 2007; Jarvis et al., 2011; Jenkyns et al., 2017; O'Connor et al., 2020). The Eastbourne section was previously studied for calcareous nannofossil quantitative data by Lamolda et al. (1994), Paul et al. (1999) and Linnert et al. (2011) and for biostratigraphy by Tsikos et al. (2004) and Petrizzo et al. (2025). Here, we present quantitative and morphometric data of *E. floralis* performed on the same samples studied for morphometries by Faucher et al. (2017) to assess the effects of OAE 2 perturbations.

2. Eastbourne (UK)

The Eastbourne section in southeast England (UK) is one of the most expanded and well-studied records of the Cenomanian/Turonian boundary interval (CTBI), particularly for OAE 2. This section was deposited in the Anglo-Paris Basin at a paleolatitude of ~35°N (Gale, 1995, 1996; Paul et al., 1999; Fig. 1) and consists of a 27-m-thick pelagic stratigraphic sequence divided into three main lithological Units: Grey Chalk (rhythmically bedded marly chalk), Plenus Marls (greenish-grey marls and clay-rich chalk), and White Chalk (coccolith- and calcisphere-dominated nodular limestone) subdivided in the Ballard Cliff and in the overlying Holywell Members (see Gale et al., 2005 and references therein). Samples for this study were collected at Gun Gardens.

The section was biostratigraphically constrained for planktonic foraminifera (Tsikos et al., 2004; Falzoni et al., 2018) and calcareous nannofossils (Tsikos et al., 2004; Petrizzo et al., 2025) as well as through chemostratigraphy (Tsikos et al., 2004). Specifically, the characteristic positive $\delta^{13}C$ excursion of OAE 2 is recorded between the base of the Plenus Marls and the lower part of the Holywell Member and records all 4 peaks labeled "A" to "C" by Jarvis et al. (2006) and peak "D" by Voigt et al. (2007, 2008).

3. Calcareous nannofossil analyses

A total of 44 samples were prepared following the standard technique outlined by Bown and Young (1998). Quantitative and morphometric analyses were performed using a Leitz Laborlux 12 polarizing microscope at a magnification of 1250× equipped with a Deltapix light camera at the University of Milan.

For each sample, quantitative analyses were performed counting up to 300 specimens in each smear slide to assess the relative abundance (%) of *E. floralis* relative to the total number of counted specimens. Morphometric analyses were performed by taking digital pictures of 30 specimens per sample. The preservation was carefully assessed to avoid diagenetically altered specimens (partially dissolved or overgrown), if any.

Eprolithus floralis is characterized by a relatively tall, multiradiate structure with nine petaloid wall-cycle elements surrounding a broad

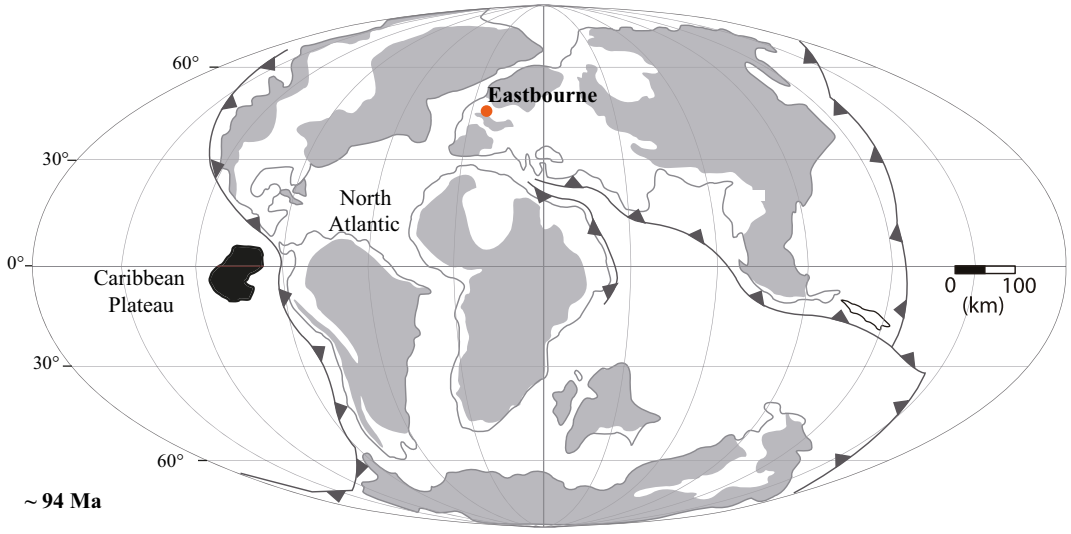

Fig. 1. Paleo-location of the Eastbourne section at approximately 94 Ma (latest Cenomanian), after Faucher et al. (2017).

central area spanned by a median diaphragm. For each specimen, the "total diameter", "inner diameter", and "diaphragm diameter" were measured with the ImageJ software using the macros by Young et al. (2014), as specified in Fig. 2.

Data were statistically elaborated in Excel and Past software version 4.03 (Hammer et al., 2001) to obtain mean, median, minimum, maximum, 95 % confidence intervals and standard deviation. Pearson correlation coefficient and *p*-value were also calculated to test any relationship between the measured parameter as well as with *E. floralis* abundance. Independent-sample *t*-tests were performed to determine whether size variations between intervals were statistically significant ($p < 0.05$). Effect sizes were quantified using Cohen's *d* (Cohen, 1988) to assess the magnitude of differences independently of sample size. One-sample *t*-tests were performed to compare interval means against reference values, such as the overall mean of the respective parameter. Results of statistical analyses are reported in the Supplementary Data Appendix A, Supplementary Fig. S1 and Table S1.

Reduction rates were calculated to highlight size variation and to compare the similar or different patterns of the three parameters considered.

4. Results

The morphometric analysis revealed variations in the three measured parameters (Fig. 3). The total diameter shows an average of 6.3 ± 0.8 μm, ranging from an average minimum of 5.4 μm to a maximum of 7.2 μm, differing by nearly 2 μm. The smallest specimen detected is 3.6 μm whereas the largest is 8.8 μm in total diameter. The ratio between internal variability (sdv ≈ 0.8 μm) and variability across samples (range ≈ 1.8 μm) suggests that the observed differences among samples are not due to statistical noise but possibly reflect primary variations.

Before OAE 2 specimens are relatively larger (average 6.6 μm), while smaller specimens occur during OAE 2 (average 6.1 μm). The smallest *E. floralis* specimens are around peak B (average 6 μm). After peak C, specimen size starts to increase, and largest specimens are detected above peak D (average 6.9 μm) (Fig. 3).

The inner diameter ranges from a minimum average of 4.8 μm to a maximum average of 5.9 μm, with a total average of 5.3 ± 0.70 μm. The overall variability among samples (range ≈ 1.1 μm) is higher than the variability within individual samples. This ratio between within-sample variability and between-sample variation suggests that the observed changes in inner diameter possibly reflect genuine differences rather than random noise. Fluctuations of the inner diameter follow those of the total diameter and show higher values prior to OAE 2 (average 5.6 μm) while smaller average size (5.2 μm) is detected within the OAE 2 interval, with the smallest average (5.1 μm) between peak A and peak B. After peak C, the inner diameter starts to increase and largest values are observed above peak D (average 5.6 μm), (Fig. 3).

t-tests and Cohen's *d* values calculated on total and inner diameters indicate that the size variations observed from pre-OAE 2 to OAE 2 and afterward are statistically significant (Supplementary Table S1). The total and the inner diameters display similar patterns and are highly correlated ($r = 0.940$; $p < 0.001$, Supplementary Fig. S1).

The diaphragm diameter has an average value of ~3 ± 0.43 μm, ranging from 2.6 μm to 3.2 μm, and shows fluctuations of very minor amplitude. Standard deviation range 0.25–0.54 μm is of comparable magnitude to the variability between samples (≈ 0.65 μm) suggesting that observed differences may largely reflect within-sample variability rather than systematic shifts. Slightly larger values were detected in the OAE 2 interval, except around peak B where the diaphragm diameter is smaller in average (ca. 2.6 μm), (Fig. 3). Smaller diaphragm diameter values occur above peak C with average of 2.8 μm. t-tests indicate that only the size variation from OAE 2 to post-OAE 2 is significant (Supplementary Table S1). No correlation was observed between the diaphragm diameter and the total diameter ($r = 0.227$, Supplementary Fig. S1) and between the diaphragm diameter and the inner diameter ($r = 0.332$, Supplementary Fig. S1).

Two distinct morphotypes were observed, each exhibiting a specific shape of the termination of the elements: the spiky morphotype is characterized by more elongated and pointed elements, whereas the rounded morphotype exhibits shorter and rounded elements (Fig. 3, Plate 1). The two morphotypes show differences in average size, size patterns, and relative abundance, as follows.

***Rounded* morphotype**: among *E. floralis* specimens, the average abundance of *rounded* morphotype is 64 % (Fig. 4). This morphotype is more abundant during OAE 2 (76 %) compared to pre- (39 %) and post-OAE 2 (44 %) intervals (Fig. 4). In particular, rounded specimens constitute 83 % of the total *E. floralis* in the interval comprised between the base of the first buildup of the CIE and just above peak B. In this interval the average of the total diameter of the *rounded* morphotype is relatively low, being ~6.2 ± 0.80 μm. The total diameter of this morphotype ranges from a minimum average value of 5.4 μm to a maximum average of 8.1 μm (Fig. 3). The inner diameter (average) ranges from a minimum average of 4.7 μm to a maximum average of 6.9 μm with average of 5.2 ± 0.69 μm. The average diaphragm length is 3 ± 0.42 μm, ranging from 2.5 μm to 3.2 μm. Prior to OAE 2, specimens of the *rounded* morphotype are larger (average 6.4 μm), and the smallest specimens were observed between peak A and B where the mean total diameter is 5.9 μm. After peak B specimens show a recovery in the average size and above OAE 2 reach the largest average total diameter (6.9 μm) but have smaller average diaphragm (2.9 μm) compared to the average prior to

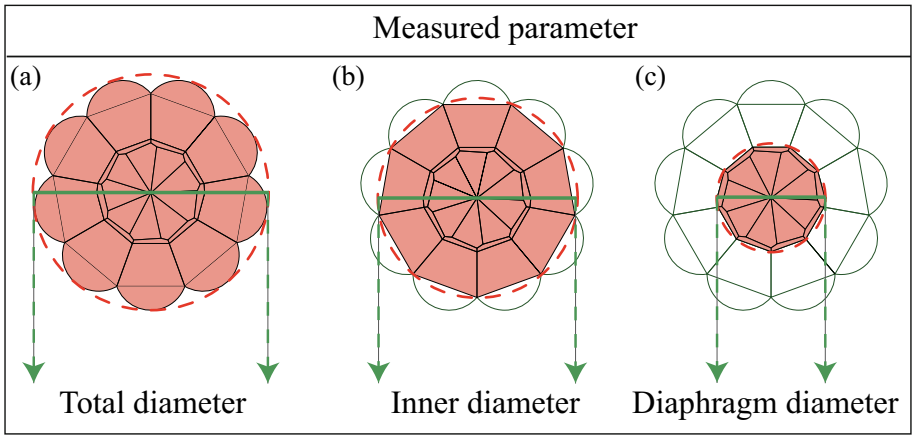

Fig. 2. Morphometric parameters measured in *Eprolithus floralis*: a) Total diameter: The circumference diameter encompassing the specimen. b) Inner diameter: the diameter of the circumference tangent to the intersection of the petals. c) Diaphragm diameter: The diameter of the diaphragm.

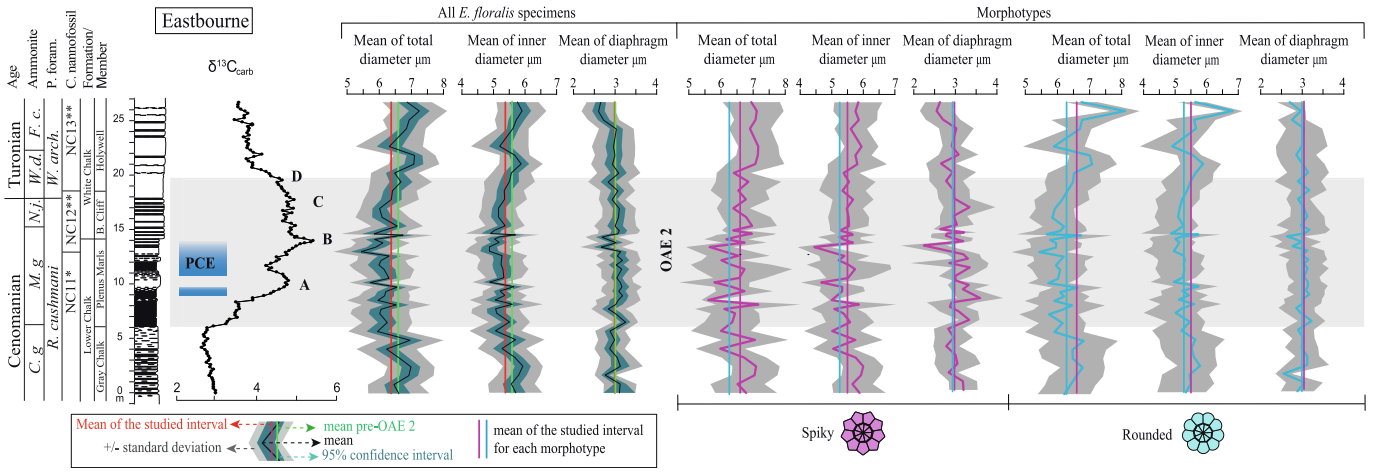

Fig. 3. Eastbourne (Gun Gardens) section, SE England. $\delta^{13}C_{carb}$ is according to Tsikos et al. (2004). Ammonite stratigraphy is after Gale et al. (2005); Planktonic foraminifera biozones are from Falzoni and Petrizzo (2020). Calcareous nannofossil biozones follows Tsikos et al. (2004) and Petrizzo et al. (2025). Peaks A, B, C and D after Jarvis et al. (2006) and Voigt et al. (2008). Plenus Cold Event (PCE) interval after Jenkyns et al. (2017). Morphometries of *Eprolithus floralis* (dark green), *rounded* morphotype (light blue), and *spiky* morphotype (pink) are from this work. (For interpretation of the references to colour in this figure legend, the reader is referred to the web version of this article.)

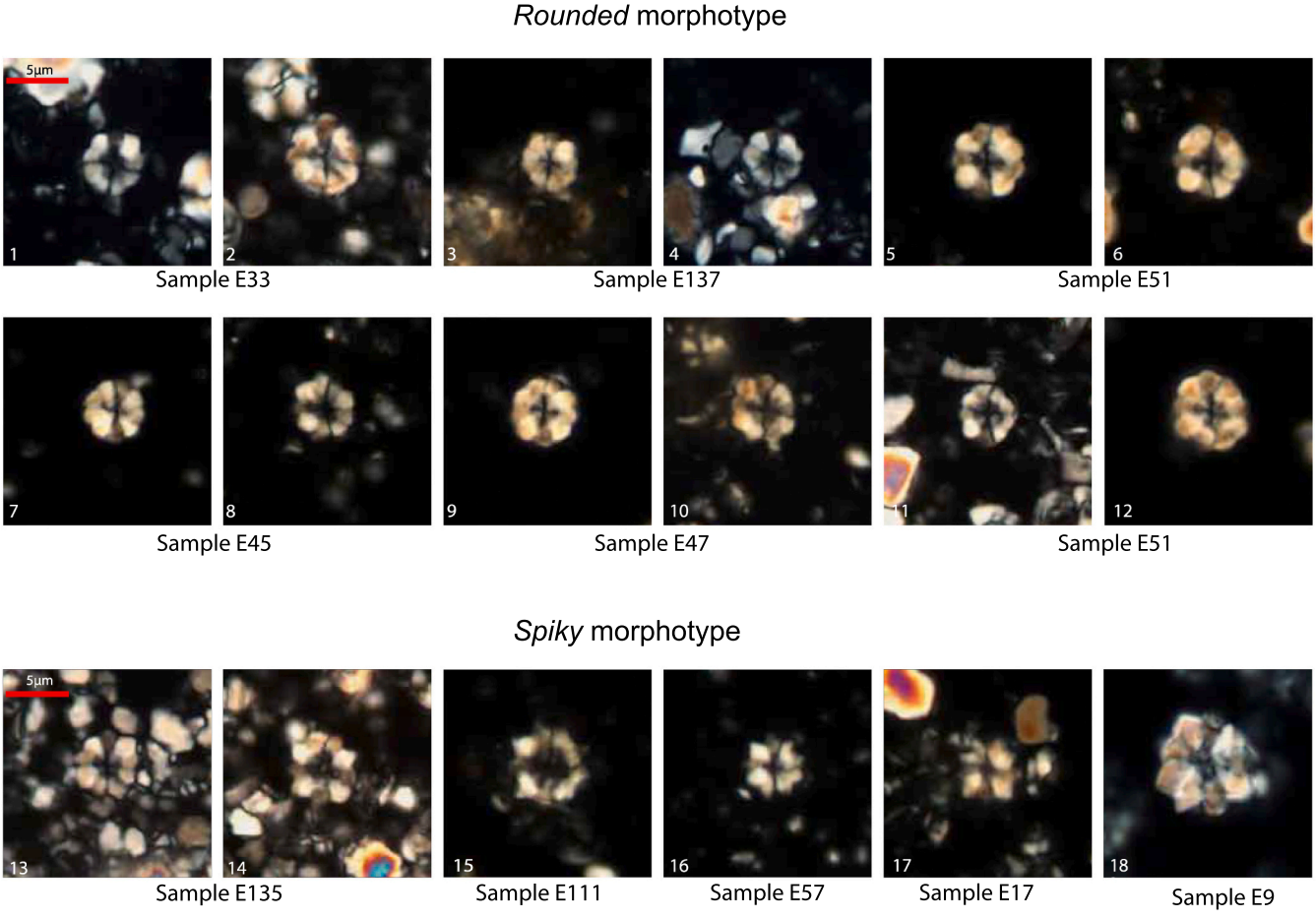

Plate 1. *Eprolithus floralis* specimens from Eastbourne (Gun Gardens) section, SE England photographed with the light polarizing microscope under cross-polarized light. Specimens 1 to 12 are *rounded E. floralis* morphotype, specimens from 13 to 18 are *spiky E. floralis* morphotype.

and during OAE 2 (3 µm). Size variations observed from pre-OAE 2 to OAE 2 and afterward are statistically significant (Supplementary Table S1).

***Spiky* morphotype:** among *E. floralis* specimens, the average abundance of the *spiky* morphotype is 37 % with highest values prior to and after OAE 2, representing 61 % and 56 % of the total *E. floralis*,

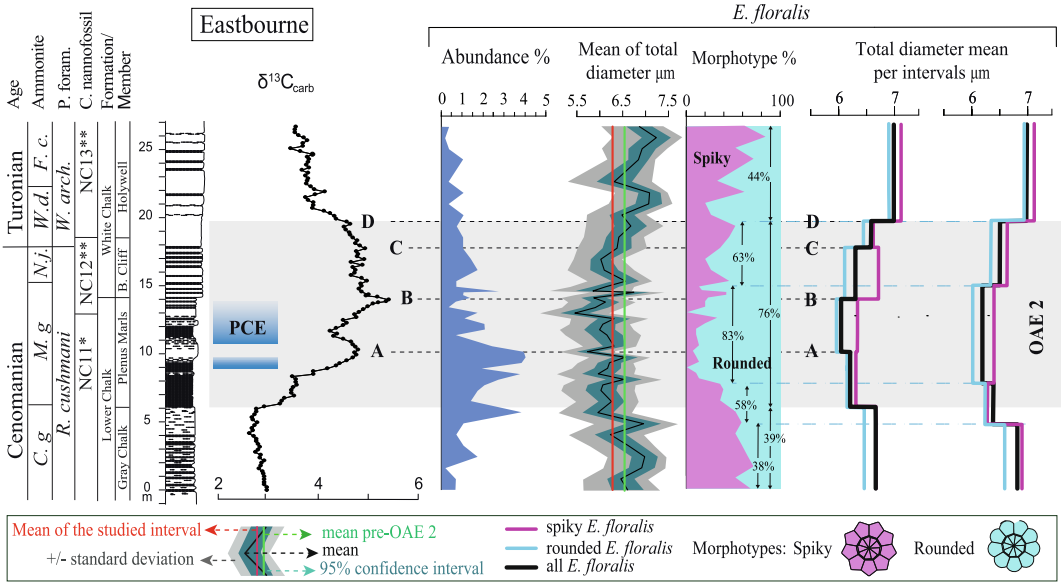

Fig. 4. Eastbourne (Gun Gardens) section stratigraphy as in Fig. 3. *Eprolithus floralis* total relative abundance (%), total diameter size and relative abundances of *rounded* and *spiky* morphotype (% of the total *E. floralis* pool) are from this work. Mean of total diameter of *spiky* (pink), *rounded* (blue) and all specimens (black) divided per interval, specifically: in the left graph, intervals follow the stratigraphy (pre-OAE 2; base of OAE 2 – peak A; peak A - peak B; peak B - peak C; peak C - peak D; after OAE 2); on the right graph, intervals follow those of morphotype abundances indicated with the dashed blue horizontal lines. (For interpretation of the references to colour in this figure legend, the reader is referred to the web version of this article.)

respectively (Fig. 4). A decrease in relative abundance is observed in the OAE 2 interval, where the *spiky* specimens account for 24 % of the total *E. floralis*. This morphotype shows a total diameter average of ~6.7 ± 0.81 µm, ranging from 5.6 µm to 7.1 µm (Fig. 3). The inner diameter (average of 5.5 ± 0.69 µm) ranges from average values of 4.4 µm to 6 µm. The diaphragm diameter ranges from average values of 2.2 µm to 3.6 µm, with a total average of 2.9 ± 0.40 µm. The *spiky* specimens have larger total and inner diameter before OAE 2 (average total diameter 6.6 µm, inner diameter 5.6 µm) and show a moderate size decrease from the OAE 2 onset to peak B (average total diameter 6.3 µm, inner diameter 5.3 µm). After peak B the average total and inner diameters are characterized by a marked recovery in size reaching values similar to those of the pre-OAE 2 interval. Largest *spiky* specimens are detected after OAE 2 (average total diameter 7 µm, inner diameter 5.8 µm). Most of total and inner diameter size variations have resulted to be significant (Supplementary Table S1). The diaphragm average diameter is similar prior to and during OAE 2 (2.9 µm and 3 µm, respectively) whereas it decreases above OAE 2 down to an average of 2.7 µm, which is the only statistically significant diaphragm size variation (Supplementary Table S1).

For both morphotypes, the total and inner diameter are the only parameters showing significant correlation, with strong linear relationships ($r = 0.924$ for the *spiky* and $r = 0.947$ for the *rounded*), (Supplementary Fig. S1).

The relative abundance of all *E. floralis* specimens ranges from 0.3 to 4 % with an average of 1.4 %. The highest percentages (4 %) correspond to the lower part of the Plenus Marls between the OAE 2 onset and peak A. Lower relative abundances correspond to the upper part of the Plenus Marls, Ballard Cliff Member and the Holywell Member (Fig. 4).

A moderate negative correlation is displayed between *E. floralis* relative abundance and size, indicating that several samples with more abundant *E. floralis* are also those with the smallest specimens (Supplementary Fig. S1).

The subdivision into two morphotypes shows that the *rounded E. floralis* is significantly smaller than the spiky morphotype ($p < 0.001$; Supplementary Table S1), with an average size difference of ~0.5 µm and becomes more abundant during OAE 2. Notably, the *rounded* morphotype begins to increase in relative abundance just prior to the onset of OAE 2, comprising 58 % of the *E. floralis* population, and reaches its peak dominance (83 %) from the base of the CIE to just above peak B. Following peak B, the *spiky* morphotype gradually increases in relative abundance and eventually dominates again after OAE 2, accounting for 56 % of the *E. floralis* assemblage (Fig. 4).

The prevalence of the *rounded* morphotype during OAE 2 significantly affects the overall size trends of *E. floralis*, largely driving the observed ~6 % reduction in both total and inner diameters during this interval. In contrast, the *spiky* morphotype primarily controls the average size of *E. floralis* populations before and after OAE 2, exhibiting total diameter values that are 3.4 % and 8.4 % larger than the total average, respectively (Fig. 5a, Supplementary Fig. S2).

Importantly, the spiky morphotype exhibits only a minor size reduction during OAE 2 (−2.8 %), with average sizes remaining relatively stable from the onset of OAE 2 through peak B (Fig. 5b, Supplementary Fig. S2). This stability is further supported by *t*-tests, which indicate no statistically significant variation in total diameter and only minor variation in inner diameter (Supplementary Table S1). Conversely, the *rounded* morphotype displays a stepwise size decline, with a 5.2 % reduction in the total diameter at the onset of OAE 2 and a further 2.9 % decrease between peaks A and B, where the smallest sizes are recorded. A recovery in size of the *spiky* morphotype occurs just above peak B (+5.4 %), while the *rounded* morphotype exhibits its main size increase at peak C (+5.5 %).

In both morphotypes, the diaphragm diameter displays a contrasting trend compared to the total and inner diameters. In the OAE 2 interval, diaphragm values increase by approximately 1 % relative to pre-OAE 2 sizes (although not statistically significant, Fig. 5, Supplementary Table S1), followed by a significant 5 % decrease after OAE 2 (Fig. 5, Supplementary Table S1). These variations result in specimens that change in size and shape over time as follows.

In the pre-OAE 2 interval, both *spiky* and *rounded* morphotypes are, on average, relatively large, with diaphragm diameters close to the total average (Fig. 6). During OAE 2, up to peak B, the *spiky* morphotype becomes slightly smaller but exhibits a moderately larger diaphragm, while the *rounded* specimens are significantly smaller and with a larger diaphragm. From just after peak B to the end of OAE 2, the *spiky* morphotype tends to be larger and continues to show an enlarged diaphragm, whereas the *rounded* specimens follow a similar trend only from

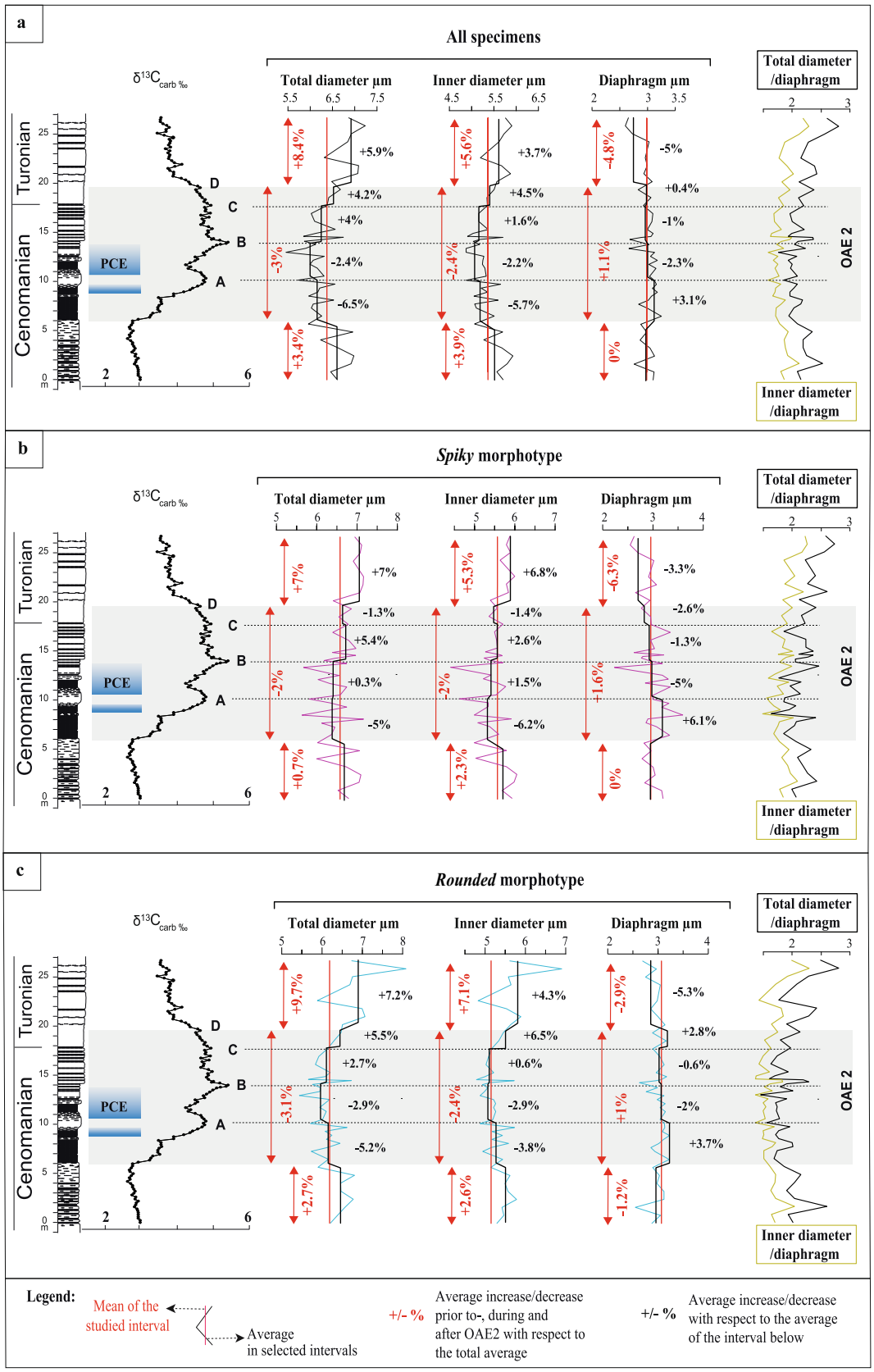

Fig. 5. Eastbourne, stratigraphy as in Fig. 3 Increase/decrease in % of all *E. floralis* specimens (a), *spiky* (b) and *rounded* (c) with respect to total mean of the studied interval (red) and with respect to the averages of the intervals marked by the base of OAE 2, peak A, B, C and D (black). Total diameter/diaphragm ratio (black) and inner diameter/diaphragm (yellow) of (a) all *E. floralis* specimens, (b) *spiky* and (c) *rounded*. (For interpretation of the references to colour in this figure legend, the reader is referred to the web version of this article.)

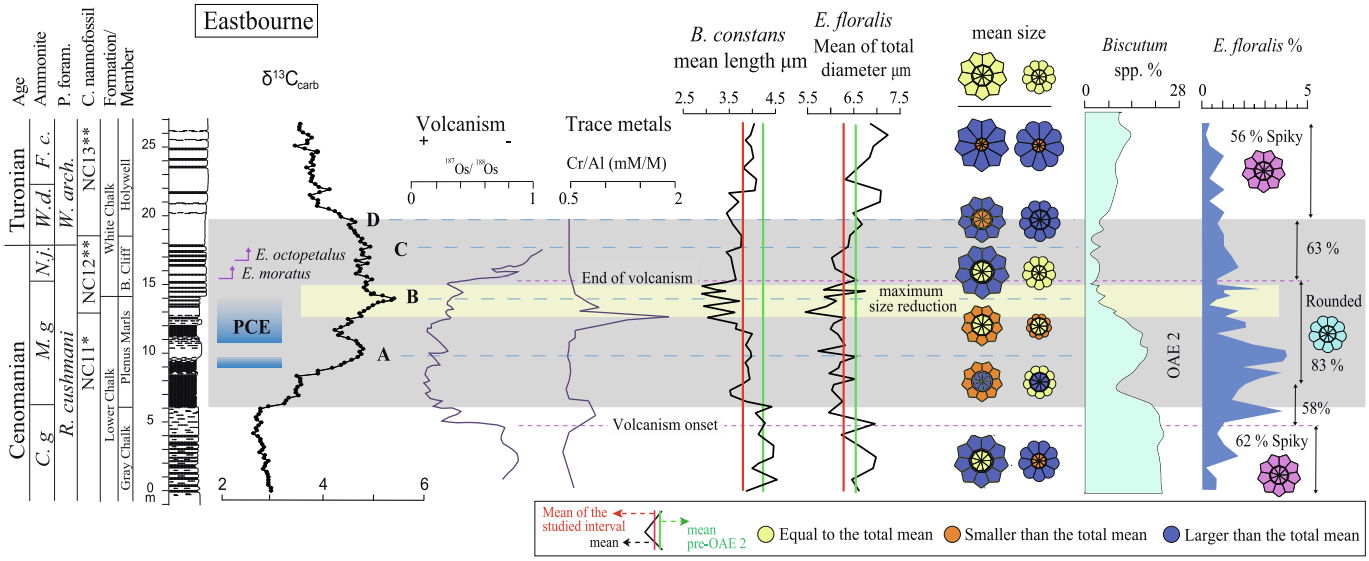

Fig. 6. Eastbourne stratigraphy as in Fig. 3. $Os_{(i)}$ from the Vocontian Basin (Du Vivier et al., 2014). Trace metals - Cr/Al (Pearce et al., 2009). *Biscutum constans* size after Faucher et al. (2017) and relative abundance after Linnert et al. (2011). *Eprolithus floralis* data (this work). First Occurrence of *Eprolithus moratus* and *E. octopetalus* from Petrizzo et al. (2025). Drawings of the two *E. floralis* morphotypes showing size variations across the intervals discussed in the text, relative to the overall mean dimensions (in yellow), are reported. (For interpretation of the references to colour in this figure legend, the reader is referred to the web version of this article.)

just after peak C upwards. In the post-OAE 2 interval, both morphotypes are larger than they were before OAE 2 and display notably smaller diaphragms. Among the two *E. floralis* morphotypes, the *rounded* one seems to be more sensitive, showing greater size variation but also appearing better adapted to OAE 2 conditions as evidenced by higher relative abundance. Conversely, the *spiky* morphotype seems to prefer the more stable conditions of the interval before and after OAE 2 and exhibits smaller size fluctuations.

5. Discussion

5.1. Nannofossil preservation

The assessment of potential dissolution effects on the morphometric variations and relative abundances of *E. floralis* and its morphotypes is particularly critical during OAE 2, an interval known, in some localities, to be associated with selective (e.g., Wunstorf section, Linnert et al., 2010) or even complete (e.g. Bonarelli Level in the Umbria-Marche Basin, Italy, Erba et al., 2019 and reference therein) dissolution of the nannoflora. Such an evaluation is essential to rule out diagenetic overprint as the primary driver of the observed patterns. Here, we present several lines of evidence supporting the interpretation that size variations recorded at Eastbourne primarily reflect a biotic response.

a) The general preservation of calcareous nannofossils in the studied samples of Eastbourne, is moderate-good to good. Calcareous nannofossils exhibit minor etching and overgrowth and delicate taxa such as *B. constans, Z. erectus* and *D. ignotus* are present throughout the studied interval (Linnert et al., 2011; Faucher et al., 2017). According to the diversity indices (species richness and Shannon Index of Linnert et al., 2011) there are only minor variations in nannofossil preservation with slightly poorer preservation observed only within the lower part of the Ballard Cliff Member.
b) Samples with the lowest total nannofossil abundances, located in the lower part of the Ballard Cliff Member, contain at least 10 % of small-sized taxa such as *B. constans* and *D. ignotus* (Linnert et al., 2011) and do not coincide with lowest average sizes of *E. floralis*, nor with shifts in the relative abundance of *spiky* versus *rounded* morphotypes. Notably, the rounded morphotype begins to increase in abundance just before OAE 2 and gradually peaks from just below peak A to ca. peak B — thus not coinciding with the OAE 2 onset or with the intervals of lowest nannofossil abundance. This pattern argues against preservation as the primary driver of the enrichment of *rounded* forms. Moreover, the co-occurrence of both morphotypes indicates that shape is primarily biologically controlled rather than the result of selective dissolution.
c) Under the assumption that diagenetic dissolution preferentially affects the outer portions of nannoliths, a reduction in total diameter would be expected while the inner diameter would remain unaltered or less impacted. Consequently, the two parameters should display a weak or negligible correlation. The data, however, show a strong positive correlation between total and inner diameter also across both *spiky* and *rounded* morphotypes, further reinforcing a primary biogenic rather than diagenetic control.
d) *Eprolithus floralis* size changes do not correspond systematically with lithological shifts. The decrease in mean size begins before the base of the Plenus Marls, minimum size values occur within the Plenus Marls, and recovery in size starts in the middle part of the Ballard Cliff Member. Overall, there is no clear one-to-one correspondence between smaller mean sizes and lithology (marlstones vs. chalks), further excluding a diagenetic control on size variations.

5.2. Eprolithus floralis size and abundance

Morphometric analysis of *E. floralis* across OAE 2 reveals significant size variation and the co-occurrence of two distinct - *spiky* and *rounded* – morphotypes, each characterized by different mean dimensions and relative abundances.

Compared to *B. constans* (Faucher et al., 2017), both the overall dimensions of *E. floralis* and those of the *rounded* morphotype display broadly similar size patterns, particularly around peak B where minimum average sizes are recorded. Outside this interval, however, size fluctuations differ partially, possibly reflecting varying sensitivities and response times (Fig. 6). For instance, *E. floralis* begins to decrease in size slightly before the onset of OAE 2, whereas *B. constans* shows a size reduction right at the onset of the event. The recovery phase of *B. constans* begins between peaks B and C, and the full recovery occurs after peak D whereas the size of *E. floralis* shows an increase surpassing

average values at peak C. In the post-OAE 2 interval, *B. constans* does not return to pre-OAE 2 size, while *E. floralis* clearly exceeds the dimensions characteristic of the pre-OAE 2 interval.

It is therefore of remark that, despite the distinct paleoecological affinities of *B. constans* and *E. floralis*, both taxa experienced an almost synchronous maximum reduction in size at peak B (Fig. 6), which is unlikely to be coincidental.

As *E. floralis* is considered a cold-water species, its abundances would be expected to increase across the PCE. Indeed, *E. floralis* is generally more abundant within the Plenus Marls (in agreement with Lamolda et al., 1994, and Paul et al., 1999), but peak values occur only during the initial build-up of the CIE (prior to and at peak A), corresponding to the early part of the PCE. In contrast, relative abundances decrease during the $\delta^{13}C$ trough—despite the PCE—arguing against temperature as the primary driver in this interval close to peak B (Fig. 6).

According to literature data (e.g. Kuroda et al., 2007; Turgeon and Creaser, 2008; Du Vivier et al., 2014; Schröder-Adams et al., 2019; Jones et al., 2023), volcanism linked to the Caribbean Plateau Large Igneous Provinces, began approximately 23,000 years before the onset of OAE 2 and reached peak intensity between the start of OAE 2 and carbon isotope peak B, with the climax occurring at peak B. Estimates of CO_2 concentrations indicate elevated levels during this interval, likely contributing to ocean acidification and global warming.

It is possible that, as previously proposed for *B. constans* alongside with other species such as *Discorhabdus rotatorius*, and *Zeugrhabdotus erectus* (Faucher et al., 2017), ocean acidification exerted control over the calcification of *E. floralis*, temporarily favoring the emergence of smaller specimens, possibly better adapted to stressful conditions. Notably, using geochemical evidence (Du Vivier et al., 2014) there is a clear correspondence between the onset of volcanism and the initial reduction in *E. floralis* size, as well as the increased relative abundance of the *rounded* morphotype (Fig. 6). Indeed, at the waning of volcanic activity (between peaks B and C) presumably CO_2 emissions started to decline and the average size of the *rounded E. floralis* began to increase, trending back toward pre-OAE 2 values.

This supports the idea that, similarly to *B. constans* (Faucher et al., 2017), *E. floralis* produced smaller specimens as a physiological strategy to cope with increased ocean acidification. It is noteworthy that the most pronounced size reductions in both species occurred at peak B, which corresponds with the period of most intense volcanic activity, highest atmospheric CO_2 concentrations, and maximum trace metal enrichments (e.g., Snow et al., 2005; Förster et al., 2007; Jarvis et al., 2011; Zheng et al., 2013; Du Vivier et al., 2014; Jenkyns et al., 2017; O'Connor et al., 2020; Percival et al., 2020).

The delayed size recovery in *B. constans* compared to *E. floralis* may reflect a higher sensitivity of *B. constans* to altered seawater chemistry, with its recovery in size occurring around peak D at the end of OAE 2. The new dataset confirms that *B. constans* was a highly responsive species (e.g., Erba et al., 2010; Lübke et al., 2015; Faucher et al., 2017; Bottini and Faucher, 2020; Möller et al., 2020) as its size fluctuations are more pronounced compared to other coccoliths (*W. barnesiae*) and nannoliths (*E. floralis*).

A decrease in size and abundance of specific nannofossils during OAEs is not novel and has been observed in heavily calcified nannoliths, such as *Schizosphaerella* during the T-OAE (e.g. Mattioli and Pittet, 2002; Suan et al., 2008, 2010; Mattioli et al., 2009; Reolid et al., 2014; Clémence et al., 2015; Peti and Thibault, 2017; Erba et al., 2019; Menini et al., 2021; Peti et al., 2021; Faucher et al., 2022), and the nannoconids during the Weissert Event (Erba and Tremolada, 2004; Barbarin et al., 2012; Erba and Parente, 2025) and OAE 1a (Erba, 1994; Erba and Tremolada, 2004; Erba et al., 2019; Erba and Parente, 2025). In these three cases, the abundance crises and/or size reduction was interpreted as the response to CO_2 excess in the ocean/atm system. At Eastbourne, OAE 2 is marked by a decrease in size and abundance of *E. floralis*, partially resulting in the dominance of the smaller *rounded* morphotype and extremely low abundances of the larger *spiky* specimens. The patterns exhibited by *E. floralis* during OAE 2 resemble those observed in *Schizosphaerella* during the T-OAE (Faucher et al., 2022), with smaller specimens becoming dominant over larger ones. What emerges from the data collected in this study is that different nannofossil species exhibited varying levels of sensitivity and adaptive capacity, employing strategies that were sometimes similar but not identical, possibly in response to the specific environmental conditions. A common adaptive response among several taxa, including *E. floralis*, appears to be a reduction in calcification, which likely served as an effective strategy to cope with elevated CO_2 levels and broadly stressed environmental conditions.

The presence of two morphotypes of *E. floralis* across OAE 2 may also be discussed in the broader context of speciation within the genus *Eprolithus*, which underwent a progressive reduction in the number of petal elements beginning in the second part of OAE 2. In the late Cenomanian, *E. floralis* is characterized by nine petals, but during OAE 2 this number steadily decreases, giving rise to *E. octopetalus* (eight petals) and *E. moratus* (seven petals). This evolutionary trend highlights the dynamic response of Polycyclolithaceae during the calcareous nannofossil turnover associated with the C/T boundary. At Eastbourne, the first occurrences (FOs) of *E. octopetalus* and *E. moratus* fall between peak B and peak C (Fig. 6).

These observations may suggest that the genus *Eprolithus* was particularly prone to both size and morphological changes, and it is noteworthy that such variability emerges after peak B. A possible interpretation is that the appearance of these new species, along with the trend toward larger *E. floralis*, reflects an adaptive response to more favorable conditions—perhaps linked to changes in water chemistry—following the cessation of intense volcanism. However, it should be noted that the FOs of *E. octopetalus* and *E. moratus* are diachronous among OAE 2 sections (Petrizzo et al., 2025), making it difficult at this stage to establish a direct causal link between speciation and environmental stress. The underlying drivers therefore remain uncertain.

6. Conclusions

Morphometric data indicates that *E. floralis* responded to OAE 2 through adaptive changes consisting in reduced average size and changes in relative abundance. Two distinct morphotypes of *E. floralis* were identified: a *rounded* form, on average 0.5 μm smaller, which dominates during OAE 2, and a *spiky* form, which is prevalent before and after the event.

The observed size decrease of *E. floralis* across OAE 2 was largely driven by the *rounded* morphotype, whose relative abundance began to increase just prior to the event, coinciding with the onset of volcanism associated with the Caribbean Plateau. The end of volcanism coincided with the increase in abundance of larger spiky *E. floralis* specimens characterized by a relatively smaller diaphragm, especially after OAE 2, compared to pre-OAE 2 forms.

The morphometric trends of *E. floralis* broadly parallel those of other coccoliths, such as *B. constans*, though with lower sensitivity in terms of the magnitude of size reduction. Notably, the recovery of *E. floralis* to pre-OAE 2 sizes occurred earlier than that of *B. constans*, possibly indicating a greater resilience to environmental perturbations.

The lack of correspondence between *E. floralis* abundance patterns and the cooling phases of the Plenus Cold Event (PCE) indicates that its abundance was not directly controlled by temperature decline. Indeed, during the core of the PCE, *E. floralis* showed a reduction in size, concurrent with *B. constans*, most likely reflecting a response to peak environmental stress rather than to cooling.

Significantly, the size and abundance variations of *E. floralis* differ from those observed in other heavily calcified nannoliths across different OAEs and only resemble the adaptive response of *Schizosphaerella* during the Toarcian Oceanic Anoxic Event (T-OAE), when larger morphotypes temporarily disappeared in favor of smaller, presumably more stress-tolerant forms.

Thus, overall, this study confirms that *E. floralis*, like other calcareous

nannoplankton, adopted a reduction in calcification to survive CO_2 excess and environmental stress during OAE 2. However, its specific response highlights the taxon-specific nature of nannofossil adaptation across global perturbation events.

Funding sources

The work was funded by European Union – Next Generation EU PRIN MUR 2022WEZR44 to C. Bottini and partly supported by the Italian Ministry for Universities and Research (MUR) through the project "Dipartimenti di Eccellenza 2023-27".

CRediT authorship contribution statement

Edna de Jesus Francisco Tungo: Writing – original draft, Visualization, Validation, Methodology, Investigation, Formal analysis, Data curation. **Elisabetta Erba:** Writing – review & editing, Supervision, Resources, Methodology, Conceptualization. **Gerson Fauth:** Supervision, Funding acquisition. **Cinzia Bottini:** Writing – review & editing, Validation, Supervision, Resources, Project administration, Funding acquisition, Data curation, Conceptualization.

Declaration of competing interest

The authors declare that they have no known competing financial interests or personal relationships that could have appeared to influence the work reported in this paper.

Data availability

Raw data and statistical elaborations are deposited in DATAVERSE at this link https://doi.org/10.13130/RD_UNIMI/B5EFJD

Acknowledgments

We thank the Editor for managing the review process and his insightful comments. We are grateful to Dr. J. Schueth and the anonymous Reviewer for the constructive feedback that greatly helped us in revising the paper.

Edna Tungo is a fellow of Coordenação de Aperfeiçoamento de Pessoal de Nível Superior (CAPES), and thanks Conselho Nacional de Desenvolvimento Científico e Tecnológico (CNPq) for the Fellowship grant SWE 200253/2023–9 through the project 402,804/2022–8.

Appendix A. Supplementary data

Supplementary data to this article can be found online at https://doi.org/10.1016/j.marmicro.2025.102525.

References

Amaglio, G., Petrizzo, M.R., Holbourn, A., Kuhnt, W., Wolfgring, E., 2023. Benthic foraminiferal response to the Oceanic Anoxic Event 2 (late cretaceous) and evidence of bottom water re-oxygenation during the Plenus Cold Event at Clot Chevalier (Vocontian Basin, SE France). Palaeogeogr. Palaeoclimatol. Palaeoecol. 623, 111598. https://doi.org/10.1016/j.palaeo.2023.111598.

Arthur, M.A., Dean, W.E., Pratt, L.M., 1988. Geochemical and climatic effects of increased marine organic carbon burial at the Cenomanian/Turonian boundary. Nature 335 (6192), 714–717.

Barbarin, N., Bonin, A., Mattioli, E., Pucéat, E., Cappetta, H., Gréselle, B., Pittet, B., Vennin, E., Joachimski, M., 2012. Evidence for a complex Valanginian nannoconid decline in the Vocontian basin (South East France). Mar. Micropaleontol. 84, 37–53. https://doi.org/10.1016/j.marmicro.2011.11.005.

Barclay, R.S., McElwain, J.C., Sageman, B.B., 2010. Carbon sequestration activated by a volcanic CO_2 pulse during Ocean Anoxic Event 2. Nat. Geosci. 3 (3), 205–208. https://doi.org/10.1038/NGEO757.

Bice, K.L., Birgel, D., Meyers, P.A., Dahl, K.A., Hinrichs, K.U., Norris, R.D., 2006. A multiple proxy and model study of Cretaceous upper ocean temperatures and atmospheric CO_2 concentrations. Paleoceanography 21 (2). https://doi.org/10.1029/2005PA001203.

Bottini, C., Faucher, G., 2020. *Biscutum constans* coccolith size patterns across the mid Cretaceous in the western Tethys: Paleoecological implications. Palaeogeogr. Palaeoclimatol. Palaeoecol. 555, 109852. https://doi.org/10.1016/j.palaeo.2020.109852.

Bown, P.R., Young, J.R., 1998. Introduction. In: Bown, P.R. (Ed.), Calcareous Nannofossil Biostratigraphy. British Micropalaeontology Society Series, p. 1.

Bralower, T.J., 1988. Calcareous nannofossil biostratigraphy and assemblages of the Cenomanian-Turonian boundary interval: implications for the origin and timing of oceanic anoxia. Paleoceanography 3 (3), 275316. https://doi.org/10.1029/PA003i003p00275.

Bryant, R., Leckie, R.M., Bralower, T.J., Jones, M.M., Sageman, B.B., 2021. Microfossil and geochemical records reveal high-productivity paleoenvironments in the cretaceous Western Interior Seaway during Oceanic Anoxic Event 2. Palaeogeogr. Palaeoclimatol. Palaeoecol. 584, 110679. https://doi.org/10.1016/j.palaeo.2021.110679.

Clémence, M.E., Gardin, S., Bartolini, A., 2015. New insights in the pattern and timing of the early Jurassic calcareous nannofossil crisis. Palaeogeogr. Palaeoclimatol. Palaeoecol. 427, 100–108. https://doi.org/10.1016/j.palaeo.2015.03.024.

Cohen, J., 1988. Statistical Power Analysis for the Behavioral Sciences, 2nd ed. Lawrence Erlbaum Associates.

Dickson, A.J., Jenkyns, H.C., Porcelli, D., van den Boorn, S., Idiz, E., 2016. Basin-scale controls on the molybdenum-isotope composition of seawater during Oceanic Anoxic Event 2 (late Cretaceous). Geochim. Cosmochim. Acta 178, 291–306. https://doi.org/10.1016/j.gca.2015.12.036.

Dodsworth, P., 2016. Palynostratigraphy and palaeoenvironments of the Eagle Ford Group (Upper Cretaceous) at the Lozier Canyon outcrop reference section, West Texas, USA. Palynology 40 (3), 357–378. https://doi.org/10.1080/01916122.2015.1073188.

Du Vivier, A.D., Selby, D., Sageman, B.B., Jarvis, I., Gröcke, D.R., Voigt, S., 2014. Marine $^{187}Os/^{188}Os$ isotope stratigraphy reveals the interaction of volcanism and ocean circulation during Oceanic Anoxic Event 2. Earth Planet. Sci. Lett. 389, 23–33. https://doi.org/10.1016/j.epsl.2013.12.024.

Duggen, S., Olgun, N., Croot, P., Hoffmann, L., Dietze, H., Delmelle, P., Teschner, C., 2010. The role of airborne volcanic ash for the surface ocean biogeochemical iron-cycle: a review. Biogeosciences 7 (3), 827–844. https://doi.org/10.5194/bg-7-827-2010.

Eicher, D.L., Diner, R., 1985. Foraminifera as indicators of water mass in the Cretaceous Greenhorn Sea, Western Interior. In: Pratt, L.M., Kauffman, E.G., Zelt, F.B. (Eds.), Fine-Grained Deposits and Biofacies of the Cretaceous Western Interior Seaway: Evidence of Cyclic Sedimentary Processes, 4. Field Trip Guidebook, Society of Economic Paleontologists and Mineralogists, pp. 60–71.

Eicher, D.L., Worstell, P., 1970. Cenomanian and Turonian foraminifera from the Great Plains, United States. Micropaleontology 16, 269–324.

Eldrett, J.S., Minisini, D., Bergman, S.C., 2014. Decoupling of the carbon cycle during Ocean Anoxic Event 2. Geology 42 (7), 567–570. https://doi.org/10.1130/G35520.1.

Erba, E., 1992. Calcareous nannofossil distribution in pelagic rhythmic sediments (Aptian – Albian Piobbico core, Central Italy). Riv. Ital. Paleont. Strat. 97, 455–484.

Erba, E., 1994. Nannofossils and superplumes: the early Aptian "nannoconid crisis". Paleoceanography 9 (3), 483–501. https://doi.org/10.1029/94PA00258.

Erba, E., 2004. Calcareous nannofossils and Mesozoic Oceanic Anoxic Events. Mar. Micropal. 52 (1–4), 85–106. https://doi.org/10.1016/j.marmicro.2004.04.007.

Erba, E., Parente, M., 2025. The resilience of Tethyan planktonic and benthic calcifying algae to early cretaceous perturbations: Comparison between the Valanginian Weissert Event and the early Aptian Oceanic Anoxic Event 1a. Geol. Soc. Lond. Spec. Publ. 545 (1). https://doi.org/10.1144/SP545-2023-125. SP545–2023.

Erba, E., Tremolada, F., 2004. Nannofossil carbonate fluxes during the early Cretaceous: phytoplankton response to nutrification episodes, atmospheric CO_2, and anoxia. Paleoceanography 19 (1). https://doi.org/10.1029/2003PA000884.

Erba, E., Bottini, C., Weissert, H.J., Keller, C.E., 2010. Calcareous nannoplankton response to surface-water acidification around Oceanic Anoxic Event 1a. Science 329 (5990), 428–432. https://doi.org/10.1126/science.1188886.

Erba, E., Bottini, C., Faucher, G., Gambacorta, G., Visentin, S., 2019. The response of calcareous nannoplankton to Oceanic Anoxic Events: the italian pelagic record. Soc. Paleontol. Ital. 58, 51–71. https://doi.org/10.4435/BSPI.2019.08.

Falzoni, F., Petrizzo, M.R., 2020. Patterns of planktonic foraminiferal extinctions and eclipses during Oceanic Anoxic Event 2 at Eastbourne (SE England) and other mid-low latitude locations. Cret. Res. 116, 104593. https://doi.org/10.1016/j.cretres.2020.104593.

Falzoni, F., Petrizzo, M.R., Valagussa, M., 2018. A morphometric methodology to assess planktonic foraminiferal response to environmental perturbations: the case study of Oceanic Anoxic Event 2. Late Cretaceous. Boll. Soc. Paleontol. Ital. 57 (2), 103124. https://doi.org/10.4435/BSPI.2018.07.

Faucher, G., Erba, E., Bottini, C., Gambacorta, G., 2017. Calcareous nannoplankton response to the latest Cenomanian Oceanic Anoxic Event 2 perturbation. Riv. Ital. Paleontol. Stratigr. 123 (1), 159–176. https://doi.org/10.13130/2039-4942/8092.

Faucher, G., Visentin, S., Gambacorta, G., Erba, E., 2022. Schizosphaerella size and abundance variations across the Toarcian Oceanic Anoxic Event in the Sogno Core (Lombardy Basin, Southern Alps). Palaeogeogr. Palaeoclimatol. Palaeoecol. 595, 110969. https://doi.org/10.1016/j.palaeo.2022.110969.

Förster, A., Schouten, S., Baas, M., Sinninghe Damsté, J.S., 2007. Mid-Cretaceous (Albian–Santonian) sea surface temperature record of the tropical Atlantic Ocean. Geology 35 (10), 919–922. https://doi.org/10.1130/G23874A.1.

Gale, A.S., 1995. Cyclostratigraphy and correlation of the Cenomanian Stage in Western Europe. In: House, M.R., Gale, A.S. (Eds.), Orbital forcing timescales and

cyclostratigraphy: Geol. Soc. Spec. Pub., 85 The Geological Society, London, pp. 177–197.
Gale, A.S., 1996. Turonian correlation and sequence stratigraphy of the Chalk in southern England. In: Hesselbo, S.P., Parkinson, D.N. (Eds.), Sequence Stratigraphy in British Geology: Geol. Soc. Spec. Pub., 103 The Geological Society, London, pp. 177–195.
Gale, A.S., Kennedy, W.J., Voigt, S., Walaszczyk, I., 2005. Stratigraphy of the Upper Cenomanian–Lower Turonian Chalk succession at Eastbourne, Sussex, UK: ammonites, inoceramid bivalves and stable carbon isotopes. Cretac. Res. 26, 460–487. https://doi.org/10.1016/j.cretres.2005.01.006.
Gale, A.S., Jenkyns, H.C., Tsikos, H., van Breugel, Y., Sinninghe Damsté, J.S., Bottini, C., Mutterlose, J., 2019. High-resolution bio- and chemostratigraphy of an expanded record of Oceanic Anoxic Event 2 (Late Cenomanian–Early Turonian) at Clot Chevalier, near Barrême, SE France (Vocontian Basin). Newsl. Stratigr. 52 (1), 97–129. https://doi.org/10.1127/nos/2018/0445.
Grasby, S.E., Them II, T.R., Chen, Z., Yin, R., Ardakani, O.H., 2019. Mercury as a proxy for volcanic emissions in the geologic record. Earth Sci. Rev. 196, 102880. https://doi.org/10.1016/j.earscirev.2019.102880.
Hammer, Ø., Harper, D.A.T., Ryan, P.D., 2001. PAST: paleontological statistics software package for education and data analysis. Palaeontol. Electron. 4, 1–9.
Herrle, J.O., Pross, J., Friedrich, O., Kößler, P., Hemleben, C., 2003. Forcing mechanisms for mid-Cretaceous black shale formation: evidence from the Upper Aptian and lower Albian of the Vocontian Basin (SE France). Palaeogeogr. Palaeoclimatol. Palaeoecol. 190, 399–426. https://doi.org/10.1016/S0031-0182(02)00616-8.
Huber, B.T., MacLeod, K.G., Watkins, D.K., Coffin, M.F., 2018. The rise and fall of the Cretaceous hot greenhouse climate. Glob. Planet. Change. 167, 1–23. https://doi.org/10.1016/j.gloplacha.2018.04.004.
Jarvis, I., Lignum, J.S., Gröcke, D.R., Jenkyns, H.C., Pearce, M.A., 2011. Black shale deposition, atmospheric CO_2 drawdown, and cooling during the Cenomanian–Turonian Oceanic Anoxic Event. Paleoceanography 26, 3. https://doi.org/10.1029/2010PA002081.
Jarvis, I.A.N., Gale, A.S., Jenkyns, H.C., Pearce, M.A., 2006. Secular variation in Late Cretaceous Carbon isotopes: A new $\delta^{13}C$ carbonate reference curve for the Cenomanian–Campanian (99.6–70.6 Ma). Geol. Mag. 143 (5), 561–608. https://doi.org/10.1017/S0016756806002421.
Jenkyns, H.C., 2010. Geochemistry of Oceanic Anoxic Events. Geochem. Geophys. Geosyst. 11 (3). https://doi.org/10.1029/2009GC002788.
Jenkyns, H.C., Dickson, A.J., Ruhl, M., Van den Boorn, S.H., 2017. Basalt-seawater interaction, the Plenus Cold Event, enhanced weathering and geochemical change: deconstructing Oceanic Anoxic Event 2 (Cenomanian–Turonian, late cretaceous). Sedimentology 64 (1), 16–43. https://doi.org/10.1111/sed.12305.
Jones, M.M., Sageman, B.B., Selby, D., Jicha, B.R., Singer, B.S., Titus, A.L., 2021. Regional chronostratigraphic synthesis of the Cenomanian–Turonian Oceanic Anoxic Event 2 (OAE2) Interval, Western Interior Basin (USA): New Re-Os chemostratigraphy and $^{40}Ar/^{39}Ar$ geochronology. Bulletin 133 (5–6), 1090–1104. https://doi.org/10.1130/b35594.1.
Jones, M.M., Sageman, B.B., Selby, D., Jacobson, A.D., Batenburg, S.J., Riquier, L., Hobbs, R.W., 2023. Abrupt episode of mid-Cretaceous ocean acidification triggered by massive volcanism. Nat. Geosci. 16 (2), 169–174. https://doi.org/10.1038/s41561-022-01115-w.
Keller, G., Adatte, T., Berner, Z., Chellai, E.H., Stueben, D., 2008. Oceanic events and biotic effects of the Cenomanian–Turonian Anoxic Event, Tarfaya Basin, Morocco. Cret. Res. 29 (5–6), 976–994. https://doi.org/10.1016/j.cretres.2008.05.020.
Kuroda, J., Ogawa, N.O., Tanimizu, M., Coffin, M.F., Tokuyama, H., Kitazato, H., Ohkouchi, N., 2007. Contemporaneous massive subaerial volcanism and late cretaceous Oceanic Anoxic Event 2. Earth Planet. Sci. Lett. 256 (1–2), 211–223. https://doi.org/10.1016/j.epsl.2007.01.027.
Kuypers, M.M., Pancost, R.D., Sinninghe Damsté, J.S., 1999. A large and abrupt fall in atmospheric CO_2 concentration during Cretaceous times. Nature 399 (6734), 342–345.
Lamolda, M.A., Gorostidi, A., Paul, C.R.C., 1994. Quantitative estimates of calcareous nannofossil changes across the Plenus Marls (latest Cenomanian), Dover, England: implications for the generation of the Cenomanian-Turonian Boundary Event. Cretac. Res. 15 (2), 143–164. https://doi.org/10.1006/cres.1994.1007.
Langmann, B., Zakšek, K., Hort, M., Duggen, S., 2010. Volcanic ash as fertiliser for the surface ocean. Atmos. Chem. Phys. 10 (8), 3891–3899.
Linnert, C., Mutterlose, J., Erbacher, J., 2010. Calcareous nannofossils of the Cenomanian–Turonian boundary interval from the Boreal Realm (Wunstorf, northwest Germany). Mar. Micropaleontol. 74, 38–58.
Linnert, C., Mutterlose, J., Mortimore, R., 2011. Calcareous nannofossils from Eastbourne (southeastern England) and the paleoceanography of the Cenomanian–Turonian boundary interval. Palaios 26 (5), 298–313.
Lübke, N., Mutterlose, J., Bottini, C., 2015. Size variations of coccoliths in Cretaceous oceans a result of preservation, genetics and ecology? Mar. Micropaleontol. 117, 25–39. https://doi.org/10.1016/j.marmicro.2015.03.002.
Macdonald, F.A., Swanson-Hysell, N.L., Park, Y., Lisiecki, L., Jagoutz, O., 2019. Arc-continent collisions in the tropics set Earth's climate state. Science 364 (6436), 181–184. https://doi.org/10.1126/science.aav5300.
Mattioli, E., Pittet, B., 2002. Contribution of Calcareous Nannoplankton to carbonate deposition: a new approach applied to the lower Jurassic of Central Italy. Mar. Micropaleontol. 45 (2), 175–190. https://doi.org/10.1016/S0377-8398(02)00039-7.
Mattioli, E., Pittet, B., Petitpierre, L., Mailliot, S., 2009. Dramatic decrease of pelagic carbonate production by nannoplankton across the early Toarcian Anoxic Event (T-OAE). Global Planet. Change 65, 134–145. https://doi.org/10.1016/j.gloplacha.2008.10.018.
Menini, A., Mattioli, E., Hesselbo, S.P., Ruhl, M., Suan, G., 2021. 2021: primary versus carbonate production in the Toarcian, a case study from the Llanbedr (Mochras Farm) borehole, Wales. Geol. Soc. Lond. Spec. Publ. 514, 59–81. https://doi.org/10.1144/SP5142021-19.
Meyer, K.M., Kump, L.R., 2008. Oceanic euxinia in Earth history: causes and consequences. Annu. Rev. Earth Planet. Sci. 36 (1), 251–288. https://doi.org/10.1146/annurev.earth.36.031207.124256.
Möller, C., Bornemann, A., Mutterlose, J., 2020. Climate and paleoceanography controlled size variations of calcareous nannofossils during the Valanginian Weissert Event (early Cretaceous). Mar. Micropaleontol. 157, 101875. https://doi.org/10.1016/j.marmicro.2020.101875.
O'Brien, C.L., Robinson, S.A., Pancost, R.D., Damsté, J.S.S., Schouten, S., Lunt, D.J., Wrobel, N.E., 2017. Cretaceous sea-surface temperature evolution: constraints from TEX_{86} and planktonic foraminiferal oxygen isotopes. Earth Sci. Rev. 172, 224–247. https://doi.org/10.1016/j.earscirev.2017.07.012.
O'Connor, L.K., Jenkyns, H.C., Robinson, S.A., Remmelzwaal, S.R.C., Batenburg, S.J., Parkinson, I.J., Gale, A.S., 2020. A re-evaluation of the Plenus Cold Event, and the links between CO_2, temperature and seawater chemistry during OAE 2. Paleoceanog. Paleoclimatol. 35 (4), e2019PA003631. https://doi.org/10.1029/2019PA003631.
Orth, C.J., Attrep Jr., M., Quintana, L.R., Elder, W.P., Kauffman, E.G., Diner, R., Villamil, T., 1993. Elemental abundance anomalies in the late Cenomanian Extinction Interval: a search for the source(s). Earth Planet. Sci. Lett. 117 (1–2), 189–204. https://doi.org/10.1016/0012-821X(93)90126-T.
Ostrander, C.M., Owens, J.D., Nielsen, S.G., 2017. Constraining the rate of oceanic deoxygenation leading up to a Cretaceous Oceanic Anoxic Event (OAE-2:~ 94 Ma). Sci. Adv. 3 (8), e1701020. https://doi.org/10.1126/sciadv.1701020.
Owens, J.D., Lyons, T.W., Lowery, C.M., 2018. Quantifying the missing sink for global organic carbon burial during a Cretaceous Oceanic Anoxic Event. Earth Planet. Sci. Lett. 499, 83–94. https://doi.org/10.1016/j.epsl.2018.07.021.
Pancost, R.D., Crawford, N., Magness, S., Turner, A., Jenkyns, H.C., Maxwell, J.R., 2004. Further evidence for the development of photic-zone euxinic conditions during Mesozoic Oceanic Anoxic events. J. Geol. Soc. London 161 (3), 353–364. https://doi.org/10.1144/0016764903-059.
Paul, C.R.C., Lamolda, M.A., Mitchell, S.F., Vaziri, M.R., Gorostidi, A., Marshall, J.D., 1999. The Cenomanian–Turonian boundary at Eastbourne (Sussex, UK): A proposed european reference section. Palaeogeogr. Palaeoclimatol. Palaeoecol. 150 (1–2), 83–121. https://doi.org/10.1016/S0031-0182(99)00009-7.
Pearce, M.A., Jarvis, I., Tocher, B.A., 2009. The Cenomanian–Turonian boundary event, OAE2 and palaeoenvironmental change in epicontinental seas: new insights from the dinocyst and geochemical records. Palaeogeogr. Palaeoclimatol. Palaeoecol. 280 (1–2), 207–234. https://doi.org/10.1016/j.palaeo.2009.06.012.
Percival, L.M., Matsumoto, H., Callegaro, S., Erba, E., Kerr, A.C., Mutterlose, J., Suzuki, K., 2025. Cretaceous large igneous provinces: from volcanic formation to environmental catastrophes and biological crises. Geol. Soc. Lond. Spec. Publ. 544 (1). https://doi.org/10.1144/SP544-2023-88. SP544–2023.
Percival, L.M.E., Witt, M.L.I., Mather, T.A., Hermoso, M., Jenkyns, H.C., Hesselbo, S.P., Ruhl, M., 2015. Globally enhanced mercury deposition during the end-Pliensbachian extinction and Toarcian OAE: A link to the Karoo–Ferrar Large Igneous Province. Earth Planet. Sci. Lett. 428, 267–280. https://doi.org/10.1016/j.epsl.2015.06.064.
Percival, L.M.E., van Helmond, N.A.G.M., Selby, D., Goderis, S., Claeys, P., 2020. Complex interactions between large igneous province emplacement and global-temperature changes during the Cenomanian–Turonian Oceanic Anoxic Event (OAE 2). Paleoceanog. Paleoclimatol. 35 (10), e2020PA004016. https://doi.org/10.1029/2020PA004016.
Peti, L., Thibault, N., 2017. Abundance and size changes in the calcareous nannofossil Schizosphaerella – relation to sea-level, the carbonate factory and palaeoenvironmental change from the Sinemurian to earliest Toarcian of the Paris Basin. Palaeogeogr. Palaeoclimatol. Palaeoecol. 485, 271–282. https://doi.org/10.1016/j. palaeo.2017.06.019.
Peti, L., Thibault, N., Korte, C., Ullmann, C.V., Cachão, M., Fibæk, M., 2021. Environmental drivers of size changes in Lower Jurassic Schizosphaerella spp. Mar. Micropaleontol. 168, 102053. https://doi.org/10.1016/j.marmicro.2021.102053.
Petrizzo, M.R., Parente, M., Falzoni, F., Bottini, C., Frijia, G., Steuber, T., Erba, E., 2025. Calcareous plankton and shallow-water benthic biocalcifiers: resilience and extinction across the Cenomanian-Turonian Oceanic Anoxic Event 2. Palaeogeogr. Palaeoclimatol. Palaeoecol. 112891. https://doi.org/10.1016/j.palaeo.2025.112891.
Premoli Silva, I., Erba, E., Salvini, G., Locatelli, C., Verga, D., 1999. Biotic changes in Cretaceous Oceanic Anoxic events of the Tethys. J. Foram. Res. 29 (4), 352–370.
Reolid, M., Mattioli, E., Nieto, L.M., Rodríguez-Tovar, F.J., 2014. The early Toarcian Oceanic Anoxic Event in the external subbetic (Southiberian Palaeomargin, Westernmost Tethys)– geochemistry, nannofossils and ichnology. Palaeogeogr. Palaeocl. 411, 79–94. https://doi.org/10.1016/j.palaeo.2014.06.023.
Robinson, S.A., Dickson, A.J., Pain, A., Jenkyns, H.C., O'Brien, C.L., Farnsworth, A., Lunt, D.J., 2019. Southern hemisphere sea-surface temperatures during the Cenomanian–Turonian: Implications for the termination of Oceanic Anoxic Event 2. Geology 47 (2), 131–134. https://doi.org/10.1130/G45842.1.
Roth, P.H., Krumbach, K.R., 1986. Middle Cretaceous calcareous nannofossil biogeography and preservation in the Atlantic and Indian Oceans: implications for paleoceanography. Mar. Micropal. 10 (1–3), 235–266. https://doi.org/10.1016/0377-8398(86)90031-9.
Schlanger, S.O., Jenkyns, H.C., 1976. Cretaceous Oceanic Anoxic events: Causes and consequences. Geol. Mijnb. 55 (3–4), 179–184.
Schlanger, S.O., Arthur, M.A., Jenkyns, H.C., Scholle, P.A., 1987. The Cenomanian-Turonian Oceanic Anoxic Event, I. In: stratigraphy and distribution of organic

carbon-rich beds and the marine $\delta^{13}C$ excursion. Geol. Soc. Lond., Spec. Publ. 26 (1), 371–399. https://doi.org/10.1144/GSL.SP.1987.026.01.24.

Scholle, P.A., Arthur, M.A., 1980. Carbon isotope fluctuations in cretaceous pelagic limestones: potential stratigraphic and petroleum exploration tool. AAPG Bull. 64, 67–87.

Schröder-Adams, C.J., Herrle, J.O., Selby, D., Quesnel, A., Froude, G., 2019. Influence of the High Arctic Igneous Province on the Cenomanian/Turonian boundary interval, Sverdrup Basin, High Canadian Arctic. Earth Planet. Sci. Lett. 511, 76–88. https://doi.org/10.1016/j.epsl.2019.01.023.

Sinninghe Damsté, J.S., van Bentum, E.C., Reichart, G.J., Pross, J., Schouten, S., 2010. A CO_2 decrease-driven cooling and increased latitudinal temperature gradient during the mid-Cretaceous Oceanic Anoxic Event 2. Earth Planet. Sci. Lett. 293, 97–103.

Snow, L.J., Duncan, R.A., Bralower, T.J., 2005. Trace element abundances in the Rock Canyon anticline, Pueblo, Colorado, marine sedimentary section and their relationship to Caribbean Plateau construction and oxygen anoxic event 2. Paleoceanography 20, 3. https://doi.org/10.1029/2004PA001093.

Stover, L.E., 1966. Cretaceous coccoliths and associated nannofossils from France and the Netherlands. Micropaleontology 12, 133–167.

Stradner, H., 1962. Über neue und wenig bekannte Nannofossilienaus Kreide und Alttertiär. Sonderdruck Verhandlungen der Geologischen Bundesanstalt (Wein) 2, 363–377.

Suan, G., Mattioli, E., Pittet, B., Mailliot, S., Lécuyer, C., 2008. Evidence for major environmental perturbation prior to and during the Toarcian (early Jurassic) Oceanic Anoxic Event from the Lusitanian Basin, Portugal. Paleoceanography 23, PA1202. https://doi.org/10.1029/2007PA001459.

Suan, G., Mattioli, E., Pittet, B., Lécuyer, C., Suchéras-Marx, B., Duarte, L.V., Philippe, M., Reggiani, L., Martineau, F., 2010. Secular environmental precursors to early Toarcian (Jurassic) extreme climate changes. Earth Planet. Sci. Lett. 290, 448–458. https://doi.org/10.1016/j.epsl.2009.12.047.

Tsikos, H., Jenkyns, H.C., Walsworth-Bell, B., Petrizzo, M.R., Forster, A., Kolonic, S., Erba, E., Premoli Silva, I., Baas, M., Wagner, T., Sinninghe Damsté, J.S., 2004. Carbon-isotope stratigraphy recorded by the Cenomanian–Turonian Oceanic Anoxic Event: correlation and implications based on three key localities. J. Geol. Soc. London 161 (4), 711–719. https://doi.org/10.1144/0016-764903-077.

Turgeon, S.C., Creaser, R.A., 2008. Cretaceous Oceanic Anoxic Event 2 triggered by a massive magmatic episode. Nature 454 (7202), 323–326. https://doi.org/10.1038/nature07076.

Voigt, S., Gale, A.S., Voigt, T., 2006. sea-level change, carbon cycling and palaeoclimate during the late Cenomanian of Northwest Europe: an integrated palaeoenvironmental analysis. Cret. Res. 27 (6), 836–858. https://doi.org/10.1016/j.cretres.2006.04.005.

Voigt, S., Aurag, A., Leis, F., Kaplan, U., 2007. Late Cenomanian to Middle Turonian high-resolution carbon isotope stratigraphy: new data from the Münsterland Cretaceous Basin, Germany. Earth Planet. Sci. Lett. 253 (1–2), 196–210. https://doi.org/10.1016/j.epsl.2006.10.026.

Voigt, S., Erbacher, J., Mutterlose, J., Weiss, J., Westerhold, T., Wiese, F., Wilmsen, M., Wonik, T., 2008. The Cenomanian–Turonian of the Wunstorf section– (North Germany): global stratigraphic reference section and new orbital time scale for Oceanic Anoxic Event 2. Newsl. Stratigr. 43, 65–89. https://doi.org/10.1127/0078-0421/2008/0043-0065.

Wagreich, M., Hu, X., Sageman, B., 2011. Causes of Oxic–Anoxic Changes in Cretaceous marine environments and their implications for earth systems—an introduction. Sediment. Geol. 235 (1–2), 1–4. https://doi.org/10.1016/j.sedgeo.2010.10.012.

Yao, H., Chen, X., Yin, R., Grasby, S.E., Weissert, H., Gu, X., Wang, C., 2021. Mercury evidence of intense volcanism preceded Oceanic Anoxic Event 1d. Geoph. Res. Lett. 48 (5), e2020GL091508. https://doi.org/10.1029/2020GL091508.

Young, J.R., Poulton, A.J., Tyrrell, T., 2014. Morphology of *Emiliania huxleyi* coccoliths northwestern European shelf - is there an influence of carbonate chemistry? Biogeosciences 11, 4771–4782. https://doi.org/10.5194/bg-11-4771-2014.

Zheng, X.Y., Jenkyns, H.C., Gale, A.S., Ward, D.J., Henderson, G.M., 2013. Changing ocean circulation and hydrothermal inputs during Ocean Anoxic Event 2 (Cenomanian–Turonian): evidence from Nd-isotopes in the European shelf sea. Earth Planet. Sci. Lett. 375, 338–348. https://doi.org/10.1016/j.epsl.2013.05.053.

Zimmerman, H.B., Boersma, A., McCoy, F.W., 1987. Carbonaceous sediments and Palaeoenvironment of the Cretaceous South Atlantic Ocean. Geol. Soc. Lond. Spec. Publ. 26 (1), 271–286. https://doi.org/10.1144/GSL.SP.1987.026.01.19.